

pubs.acs.org/JACS Article

# UV-Driven Oxygen Surface Exchange and Stoichiometry Changes in a Thin-Film, Nondilute Mixed Ionic Electronic Conductor, Sr(Ti,Fe)O<sub>3-d</sub>

Emily J. Skiba,<sup>≈</sup> Haley B. Buckner,<sup>≈</sup> Channyung Lee,<sup>≈</sup> Grace McKnight,<sup>≈</sup> Rachel F. Wallick, Renske van der Veen, Elif Ertekin, and Nicola H. Perry\*



Cite This: J. Am. Chem. Soc. 2024, 146, 23265-23277



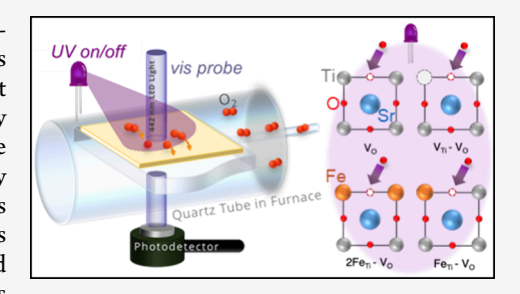
**ACCESS** I

III Metrics & More

Article Recommendations

Supporting Information

**ABSTRACT:** Enabling light-controlled ionic devices requires insight into photoionic responses in technologically relevant materials. Mixed-conducting perovskites containing nondilute Fe—serving as electrodes, catalysts, and sensors—can support large, electronically accommodated excursions in oxygen content, typically controlled by temperature, bias, and gas atmosphere. Instead, we investigated the ability of low-fluence, above-bandgap illumination to adjust oxygen stoichiometry and drive oxygen fluxes in nondilute  $Sr(Ti_{1-x}Fe_x)O_{3-x/2+\delta}$  (x=0.07,0.35) thin films with high baseline hole concentrations. Films' optical transmission at 2.8 eV was used as a probe of oxygen stoichiometry in the range  $\sim 100-500$  °C. We compared pO<sub>2</sub>-step-driven and UV (3.4 eV)-step-driven visible optical transmission relaxations



in films, finding that the time constants and activation energies of the relaxations were consistent with each other and thus with oxygen-surface-exchange-limited kinetics. Blocking oxygen exchange at the solid—gas interface with a UV-transparent capping layer resulted in no UV-induced optical relaxations. These results demonstrate that above-bandgap illumination can increase oxygen content in nondilute compositions through oxygen flux into the solid from the gas. First-principles simulations of defect formation enthalpies indicate that oxygen vacancies are energetically less favorable under steady-state illumination owing to shifts in quasi-Fermi levels. A larger 2.8 eV-optical response to UV illumination in x = 0.07 vs x = 0.35 samples was further investigated through ultrafast transient spectroscopy, where it was found that the x = 0.07 sample exhibits a slower carrier recombination. Together, these results suggest potential design principles for materials supporting large stoichiometry changes under above-gap illumination: (1) long excited carrier lifetimes and (2) highly charged, rather than neutral, defects/associates.

#### 1. INTRODUCTION

Light-mediated electronic effects in semiconductors form the basis of myriad technologies ranging from radiation detectors and photovoltaics to optical communications and various spectroscopies. For example, absorption of photons of specific energies may give rise to excited electronic carriers resulting in detectable photoconductivity, and characteristic photoemission spectra can assist in chemical analysis. A separate, albeit still electronically mediated, range of effects may be anticipated in materials that are also ionic conductors, which we term "photoionic" effects. Photoionics encompasses light-mediated changes to thermodynamic and kinetic parameters governing ion and defect fluxes. Solid-state ionic conductors (and mixed ionic/ electronic conductors) enable energy conversion/storage (batteries, fuel cells, electrolyzers), manufacturing (gas separation, thermochemical and electrochemical reactors, electrochemical nanopatterning), computing (neuromorphic architectures enabled by memristors), gas sensing, and smart devices (electrochromic windows, chemical actuators).3,4 Control over ion populations and ionic defects in these devices underlies performance-efficiency, response time, resolution, and lifetime—and is usually achieved through application of electric fields and/or ambient gas compositions/pressures. 5,6 The use of light to direct ions—photoionics—may represent a new paradigm that opens up device opportunities leveraging greater temporal or spatial control of ions wirelessly. Photoionics may be broadly divided into effects of above-band gap excitation (e.g., due to excess electron—hole pairs 7) and effects of below-gap excitation (e.g., midgap defect excitation 8 or targeted phonon stimulation 9); here we focus on the former under low photon fluences, avoiding significant thermal effects.

In mixed ionic and electronic conductors (MIECs), ionic and electronic defect and carrier populations (and their kinetics) are coupled.<sup>10</sup> Therefore, generation of excess electronic carriers, through e.g., absorption of photons with

Received: April 26, 2024 Revised: July 23, 2024 Accepted: July 24, 2024 Published: August 6, 2024





energy above the bandgap, may have consequences for ionic carrier or defect populations and kinetics.<sup>4</sup> This relationship can lead to excited-state local or global stoichiometry changes in systems with sufficient kinetic energy to allow ion transport and/or reactions internally in the lattice and/or via exchange with an external reservoir. 11 In this case, the light absorption effectively sets up a driving force (an electrochemical potential gradient) for a kinetic response involving electronic and ionic movement until a new steady-state is reached under continuous illumination. SrTiO3 is a prototypical example of a system apparently exhibiting elevated-temperature, above-gap light-induced oxygen stoichiometry changes, achieved by illumination-driven movement of oxygen. 7,12 Time-resolved measurements of electrical conductivity and color changes under UV illumination by Fleig and co-workers have been consistent with a hypothesis of oxygen entering SrTiO<sub>3</sub> (with or without dilute Fe impurities) from the gas phase under illumination at ~350-400 °C.11

Most prior studies of SrTiO<sub>3</sub> focused on thick single crystals, which convey some limitations. For example, typically the kinetic response upon illumination in O2-rich environments is consistent with a bulk oxygen diffusion limitation. 12-14 Surface reactions tend to be quicker than bulk diffusion through thick samples at elevated temperature and can be difficult to access precisely in this configuration through relaxation studies. Two reported exceptions are 1) when the bulk diffusivity is apparently enhanced over the surface exchange coefficient by UV illumination in very  $O_2$ -poor environments<sup>14</sup> or 2) sufficiently thin single crystals are employed, perhaps with a particular surface chemistry that enables slower surface exchange than bulk diffusion. The SrTiO3:Fe single crystal studies by Merkle et al. 7,15 are the only ones to report apparent surface exchange coefficients in light vs dark under typical O<sub>2</sub>rich conditions. They observed an increase in the rate of the oxygen incorporation reaction at the solid-gas interface under UV illumination when that incorporation was driven by a gasphase oxygen partial pressure increase, but there was no increase in the rate of oxygen release at the surface when the oxygen partial pressure was stepped down under UV illumination.<sup>7,15</sup> A more significant complication of thick, single-crystal studies is the impact of depth-dependent absorption, where most of the sample remains unilluminated, and a significant gradient in excess carrier generation is expected to exist with respect to depth. In that situation, given different diffusion lengths expected for excited electrons vs holes, an internal redistribution of both electronic and mobile ionic species due to the ionic photo-Dember effect may take place. This purely internal solid-phase phenomenon could be difficult to isolate from actual mass exchange with the external gas phase reservoir. The oxygen chemical potential (or quasi chemical potential) may vary in a complex way with respect to depth. 13,14 Therefore, in the present work we study thin films where a) film thickness is on the order of the absorption length, and b) kinetics are expected to be limited by oxygen surface exchange at the solid-gas interface rather than by diffusion (at least in the dark), if in fact oxygen is transferred.

One question that arises from these early studies is whether photoionic effects are limited to special compositions, or whether they may be present across a wide range of mixed conductors, including those with significant chemical substitution (e.g., solid solutions) and/or higher electronic carrier populations. In such systems, one may expect that light-induced excess carrier populations may be small relative to the

baseline carrier concentrations in the dark and that absorption depths might be shallow, leading to negligible photoionic effects of this type. However, there are several reasons to investigate nondilute systems: 1) A significant portion, if not the vast majority, of MIECs used as electrodes, channels, and membranes in practical applications are not dilute-doped compositions. 2) Nondilute systems tend to exhibit smaller/ negligible space charge effects at interfaces, such as the surface where oxygen exchange reactions take place, greatly simplifying interpretation of light-induced effects. For SrTiO<sub>3</sub> containing Fe, disappearance of an interfacial space charge effect with increasing Fe content is suggested by disappearance of blocking grain boundary arcs in impedance spectra of bulk ceramics. 16 3) Photoionics studies with systematically varying electronic structures can refine or test mechanistic understanding and inform model development. This understanding is essential to enable rational design of responsive, sensitive photoionic materials with large stoichiometry changes or kinetic responses to low photon fluences-the doorway to a new frontier of light-driven ionic devices.

In the present study we grow thin films of the nondilute compositions  $SrTi_{1-x}Fe_xO_{3-x/2+\delta}$  (x=0.07, 0.35; STF7, STF35), intermediate members of the  $SrTiO_3 - Sr_2Fe_2O_5$  solid solution with high hole concentrations. <sup>17,18</sup> At moderately elevated temperatures (~100-500 °C), we study their response to turning on or off continuous UV light with visible optical relaxations, comparing the response to optical relaxations on the same films stimulated by stepping up or down the oxygen partial pressure. The results give excellent agreement in terms of relaxation time constants and their activation energies, suggesting a common kinetic bottleneck of oxygen surface exchange. When the films are capped with a UV-transparent but O2-blocking layer, neither pO2-induced nor UV-induced visible relaxations occur. Together, the intermediate-temperature results suggest that UV illumination causes an oxygen flux from the gas phase into the film, raising the film's oxygen stoichiometry, consistent with prior reports on undoped SrTiO<sub>3</sub> single crystals. However, in contrast to one earlier report on nominally undoped SrTiO<sub>3</sub> single crystals, no effect of UV illumination on the oxygen surface exchange coefficient is observed in our nondilute thin-film compositions. To understand the initial electronic excitation, we measure the films' responses to pulsed UV light with roomtemperature ultrafast transient absorption spectroscopy. The longer decay times for STF7 vs STF35 are consistent with the larger magnitude of steady-state UV-induced visible optical relaxation at elevated temperatures in the former, and suggest that longer excited carrier lifetimes are linked to larger oxygen stoichiometry changes (when oxygen is mobile). This interpretation is also consistent with our simulations of steady-state carrier concentration changes, quasi Fermi level shifts, and oxygen stoichiometry changes for the excited vs baseline states: First-principles simulations of 10% Fe-doped SrTiO<sub>3</sub>, accounting for the formation of complexes involving Fe and native defects, suggest that changes to quasi-Fermi levels under illumination provide a thermodynamic driving force for the annihilation of V<sub>O</sub> and Fe<sub>Ti</sub>-V<sub>O</sub> with a notable reduction in the total concentration of V<sub>O</sub>

#### 2. EXPERIMENTAL SECTION

**2.1. Sample Preparation.**  $SrTi_{1-x}Fe_xO_{3-x/2+\delta}$  (x=0.07, 0.35) pellets (STF7, STF35) were prepared through solid-state synthesis, following the previously outlined procedure, <sup>19,20</sup> for use as ceramic

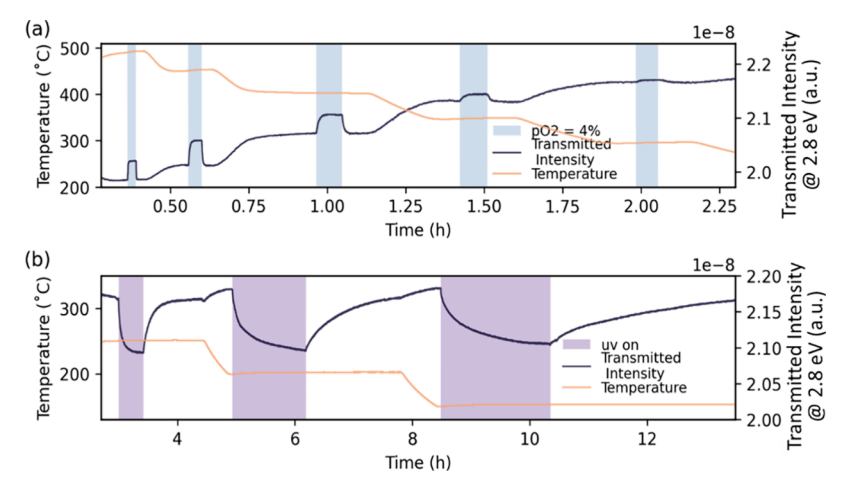


Figure 1. Example changes in transmitted light intensity at 2.8 eV as the (a) ambient pO<sub>2</sub> (0.21 vs 0.04 atm) and (b) UV illumination at 3.4 eV were stepped for a  $\sim$  440 nm-thick STF7 film on sapphire. In (b) the pO<sub>2</sub> is 0.21 atm. Note transmitted intensity represents current in A registered by the photodetector after a  $\sim$  442 nm laser line filter.

targets for pulsed laser deposition. A STF7 thin film (~440 nm thick) was deposited onto a 2-side-polished, (0001)-oriented Al<sub>2</sub>O<sub>3</sub> substrate (MTI Corp., USA). A STF35 thin film (~200 nm thick) was deposited onto a 2-side-polished, (100)-oriented 8 mol % Y<sub>2</sub>O<sub>3</sub>•ZrO<sub>2</sub> (8YSZ) substrate (MTI Corp., USA). Depositions were conducted using a 248 nm KrF excimer laser (Lambda Physik, LPX 210) in a vacuum chamber (PVD Products, nano-PLD) evacuated to a base pressure of  $3 \times 10^{-6}$  Torr. Throughout deposition, oxygen (AirGas, UHPOX 300) was introduced into the chamber at 20 sccm to maintain a process pressure of 35 mTorr, and the substrate and target were continuously rotated. The laser power, measured before entering the chamber was ~0.1 W at a pulse frequency of 5-10 Hz. Films were grown at 700  $^{\circ}\text{C}$  (set point; actual temperature  ${\sim}600~^{\circ}\text{C})$ to achieve crystallinity and assessed by out-of-plane X-ray diffraction (Bruker D8); on sapphire the film is polycrystalline with multiple outof-plane orientations (Figure S1), and on YSZ the film is (110)-oriented with columnar grains. <sup>18,21</sup> Growth rates were calibrated using X-ray reflectivity on films grown for short times under the same conditions, and final film thicknesses and compositions of the thicker samples reported here were assessed by Rutherford Backscattering Spectrometry (NEC Pelletron); see Figure S2.

To evaluate the role of surface oxygen exchange on the observed UV-induced visible optical relaxations, the deposited STF35 thin film was cut in half. The surface on one-half of the film remained pristine (i.e., no surface coatings), while a UV-transparent, amorphous alumina capping layer was deposited onto the surface of the second half to block oxygen exchange with the gas phase during measurements. The alumina coating (15 nm thick) was deposited by atomic layer deposition at 80  $^{\circ}\text{C}$  using alternating 15 ms pulses of Trimethylaluminum (TMA) and  $\text{H}_2\text{O}$  with a 30 s delay between pulses.

**2.2. Elevated-Temperature Optical Relaxation Studies.** The time dependence of optical transmission through samples at 442 nm (~2.8 eV) was monitored isothermally in controlled gas atmosphere at temperatures ranging from 100 to 500 °C using a setup described and visualized in detail previously<sup>21–23</sup> to monitor *in situ* changes in oxygen concentrations in the STF films. <sup>19,24</sup> Briefly, the films under study were held in a transparent quartz tube in a tube furnace with windows, enabling low-intensity chopped, collimated, noncoherent, and filtered (442 nm) probe light to pass through the sample, through a second laser-line filter, and into a photodetector connected to a lock-in amplifier. The gas atmosphere was controlled by mass flow controllers using UHP O<sub>2</sub> and Ar mixtures (200 sccm total flow rate, 1 atm total pressure), and rapid switches in pO<sub>2</sub> between 0.21 and 0.04 atm were accomplished using a 4-way switch with a gas flush time of ~4 s. pO<sub>2</sub>-step-induced optical relaxations of STF films were performed to assess the oxygen surface exchange kinetics. <sup>21,22,24</sup> For comparison, UV-induced optical relaxations were also studied by

turning on or off a UV LED continuously shining through the furnace window onto the whole sample area ( $\sim 1~\rm cm^2$ ). The 3.4 eV (365 nm) UV LED (LZ1–10UV0R, ams-OSRAM AG, Austria) was newly added to this optical relaxation setup, and its angle relative to the probe beam was tuned so that the UV light did not significantly impinge on the photodetector monitoring the visible light transmission (which was also blocked with a 442 nm laser line filter). The isolated effect of UV light on the measured photodetector photocurrent was tested with blank substrates. The UV LED irradiance on the films positioned in the furnace was determined to be  $\sim 10~\rm mW/cm^2$ .

For measurements on STF7 films, samples were typically heated to 500 °C in the furnace in 0.21 atm  $O_2$  (Ar balanced), and then  $pO_2$  steps and/or UV steps were conducted isothermally at each temperature; temperature was decreased between measurements in increments of ~50 °C (see, e.g., Figure 1 for an example thermal profile showing times of the  $pO_2$  steps and UV on/off switches). Conditions were maintained to allow the transmitted visible probe light intensity to reach a steady state each time before applying the subsequent  $pO_2$  UV, or temperature step. While most  $pO_2$  steps (0.21 to 0.04 atm and vice versa) were performed in the dark, some were applied while the UV light illuminated the sample, for comparison of the effect of UV light on oxygen partial pressure-driven kinetics. All UV on/off switches were conducted in 0.21 atm  $O_2$  (balance Ar).

For STF35 films, the transmitted probe light intensity responses to steps in pO $_2$  and changes in UV irradiance were evaluated at 400  $^{\circ}\text{C}$ , both for pristine films and films coated with a UV-transparent, O $_2$ -exchange-blocking layer (amorphous alumina). Once the furnace reached the 400  $^{\circ}\text{C}$  set point, the sample was annealed for 2 h to allow for equilibration at 0.21 atm. Then the transmitted light intensity (442 nm) was continuously monitored over 4 independent changes: 1) switch from 21% O $_2$  to 4% O $_2$  (reduction), 2) switch from 4% O2 to 21% O $_2$  (oxidation), 3) turn UV light on (365 nm,  $\sim$  10 mW/cm $^2$ ), and 4) turn UV light off. This process was then repeated for the sample with the amorphous alumina-capped surface.

2.3. Room-Temperature Ultrafast Transient Spectroscopy. Ultrafast UV/visible transient spectroscopy experiments were carried out using a 1 kHz Ti:sapphire regenerative amplifier (Spitfire, Spectra-Physics) located at the Materials Research Laboratory at the University of Illinois Urbana—Champaign. 800 nm pulses of approximately 100 fs with 2.5 W total output power were aligned into a TOPAS Twins (Light Conversion) and 10% of the pulse was aligned out of the TOPAS to generate the probe beam. The remaining 90% was used to generate an IR signal which was then quadrupled in a NIRUVis (Light Conversion) to generate the 343 nm pump beam (x = 0.07) or 355 nm pump beam (x = 0.35). The pump pulse was chopped at 500 Hz and was focused to a spot size of 90  $\mu$ m FWHM

using a spherical mirror. The polarization of the pump beam was not controlled. The remaining 800 nm light was passed through an optical retroreflector mounted on a motorized delay stage and passed through a  $\lambda/2$  waveplate to enable magic angle experiments. The 800 nm light was focused into a translating 3 mm crystalline CaF2 to generate the white light continuum from 300 to 700 nm. The white light was then sent through a filter to remove the remaining 800 nm light. The probe was then focused onto the sample using an off-axis parabolic mirror to a spot size of 5  $\mu$ m FWHM. The transmitted probe beam was focused into a fiber and directed into a CMOS transient absorption spectrometer (Ultrafast Systems), and data was collected shot-to-shot. The cross-phase modulation was monitored using a blank sapphire substrate and was fitted to a polynomial to correct for temporal chirp. The data sets were background subtracted by subtracting the averaged transient before the cross-phase modulation signal.

2.4. First-Principles Simulations. First-principles simulations were performed using density functional theory (DFT)<sup>25</sup> with the projector augmented wave (PAW)<sup>26</sup> method, as implemented in the Vienna Ab Initio Simulation Package (VASP).<sup>27</sup> The exchangecorrelation functional was represented by the Perdew-Burke-Ernzerhof (PBE)<sup>28</sup> formulation within the generalized gradient approximation (GGA),<sup>29</sup> augmented with a Hubbard U correction<sup>30</sup> (U = 3 eV) applied to the 3d states of Ti and Fe. The U value of 3 eV was chosen following the Fitted Elemental-phase Reference Energies (FERE) methodology,<sup>31</sup> ensuring consistency and accuracy in our calculations of thermo stability boundaries, which are essential for predicting defect formation energies. The valence electron configurations for Sr, Ti, Fe, and O were set to 10, 10, 14, and 6 electrons, respectively. Calculations employed a plane-wave basis set with a cutoff energy of 520 eV. The optimization of the bulk lattice parameter for SrTiO<sub>3</sub> resulted in a value of 3.905 Å, consistent with other PBE-based simulations and experimental findings. The calculated indirect bandgap (R to  $\Gamma$  transition) was 2.13 eV with the Hubbard U correction, compared to 1.77 eV without the correction.

Our study encompassed various native point defects, including vacancies  $(V_{Sr},V_{Ti},V_O)$ , antisite defects  $(Ti_{Sr},Sr_{Ti})$ , and native defect complexes  $(V_{Sr},V_{Ti},V_{Ti},V_O)$ ,  $V_{Sr},V_O)$ , as well as extrinsic Fe defects such as substitutions  $(Fe_{Ti})$  and Fe complexes  $(2(Fe_{Ti}),Fe_{Ti},V_O,2(Fe_{Ti}),V_O)$ . Defect structures were modeled in  $3\times3\times3$  supercells (135 atoms), with Brillouin zone sampling on a  $3\times3\times3$  k-point grid following the Monkhorst–Pack scheme. The geometries of defect structures are optimized to achieve a convergence criterion of  $1\times10^{-4}$  eV for total energy and  $2\times10^{-2}$  eV/Å for forces on atoms. Defect formation energies and charge transition levels for native and Fe-related defects in SrTiO $_3$  were determined using the standard supercell approach,  $^{33,34}$  as

$$E_{\rm f}[{\bf X}^q] = E_{\rm tot}[{\bf X}^q] - E_{\rm tot}[{\rm Bulk}] - {\rm in_i}\mu_{\rm i} + qE_{\rm Fermi} + E_{\rm corr} \tag{1}$$

In this equation,  $E_f[X^q]$  denotes the total energy of a supercell containing defect X in charge state q, whereas  $E_{\text{tot}}$  [Bulk] refers to the total energy of an equivalent pristine supercell. The difference in energy due to the addition or removal of atoms is captured by the term  $\sum_{i=1}^{\infty} n_i \mu_i$ , where  $\mu_i = \mu_i^0 + \Delta \mu_i$ , with  $\mu_i^0$  being the reference elemental chemical potential and  $\Delta\mu_i$  representing the deviation from this reference. The chemical potentials of the bulk elements were adjusted to account for finite temperature effects, using the NIST-JANAF thermochemical tables. The term  $qE_{\rm Fermi}$  accounts for the electron exchange in charged defects, with  $E_{\text{Fermi}}$  being the Fermi energy relative to the valence band maximum (VBM). To compensate for the underestimation of the band gap by the PBE functional, we adjusted our PBE band structures by expanding them to match the HSE band gap by an alignment of the average electrostatic potentials. Additionally,  $E_{\rm corr}$  serves as a correction term for defect formation energies, addressing finite-size effects within the supercell approach. This correction was estimated by following the methodology proposed by Lany and Zunger.34

Under equilibrium, the concentration of a defect (or a defect complex) carrying charge q, denoted as  $C_{D,q}$ , is

$$C_{D,q} = N_{\text{site}} \exp(-\Delta E_{D,q}/k_B T)$$
 (2)

Here,  $N_{\text{site}}$  represents the density of the defect sites available for defect formation,  $k_{\text{B}}$  is the Boltzmann constant, T is the temperature and  $\Delta E_{\text{D},q}$  is the defect formation energy. We assume defect formation energies are temperature-independent, simplifying our approach by neglecting potential contributions such as changes in vibrational entropy associated with phonons. To ensure charge neutrality at the targeted 10% Fe concentration, we determine the equilibrium Fermi energy ( $E_{\text{Fermi}}$ ) and  $\mu_{\text{Fe}}$  simultaneously. The charge neutrality equation and the Fe concentration are expressed as

$$\Sigma q C_{D,q} - n + p = 0, 10\% = \Sigma n_{Fe} C_{D,q}^{*} / N_{unit}$$
 (3)

where  $n_{Fe}$  and  $C_{D^*,q^*}$  represent the number of Fe atoms within each Fe-related defect  $(D^*)$  and their concentrations, while n and p denote the concentrations of free electrons and holes, respectively. We solve these expressions self-consistently to determine the Fe chemical potential  $\mu_{Fe}$  and the equilibrium Fermi energy  $E_{Fermi}$ .

3.1. UV- and pO<sub>2</sub>-Step Induced Optical Relaxations.

To evaluate whether the nondilute  $SrTi_{1-x}Fe_xO_{3-x/2+\delta}$  films

could undergo light-induced oxygen stoichiometry changes,

their oxygen content was monitored in situ using chopped 2.8

eV probe light at various isotherms. The transmitted 2.8 eV

#### 3. RESULTS

light intensity was monitored continuously, while the films were switched between nominally dark (furnace blackbody radiation) and light (furnace baseline plus ~10 mW/cm<sup>2</sup> of continuous ~3.4 eV UV) conditions, and/or when the pO<sub>2</sub> was switched between steady values of 0.21 and 0.04 atm. As shown in Figure 1, the x = 0.07 films exhibited significant changes in optical transmission intensity at 2.8 eV when they were exposed to UV illumination, which relaxed back to the initial transmitted intensity value after the light was turned off. This UV-induced photochromism was observed over the tested temperature range of 100 to 400 °C. Similarly, as shown in prior work, 19,21,24 the films responded optically to step changes in pO2. The transmitted light intensity decreased when stepping up to the more oxidizing 21% O<sub>2</sub> condition and when turning on the UV light. Based on earlier optical absorption measurements vs composition and density functional theory studies of the dependence of electronic structure on oxygen content, 19 this behavior is consistent with oxidation of the  $SrTi_{1-x}Fe_xO_{3-x/2+\delta}$  films. Simulations of nondilute compositions suggest that oxidation generates empty oxygenderived states at the top of the valence band that enable more

charge-transfer transitions from deeper states and increase the

subgap absorption coefficient. 19 (In dilute samples, the

increased optical absorption/decreased transmission in oxi-

dized samples is attributed to the presence of Fe<sup>4+</sup>, enabling charge transfer into a discrete Fe<sup>3+/4+</sup> level above the O 2p

valence band.<sup>36</sup>) Conversely, turning off the UV light or

stepping down the pO2 to 0.04 atm O2 resulted in an increase

in transmitted light intensity, corresponding to reduction of

the films. (Note that, in contrast to the isothermal measure-

ments, the temperature dependence of the monochromated

transmitted intensity at 2.8 eV does not directly provide insight

into redox behavior, as it also reflects temperature-dependent

energy shifts in the electronic structure and absorption

features, such as those caused by thermal expansion.)

3.2. Kinetics of UV- and pO<sub>2</sub>-Induced Optical Responses. The time-dependent behavior of the UV- and

pO<sub>2</sub> step-induced visible relaxations was analyzed to compare the films' responses to the two stimuli. For thin films with thickness (L) well below the critical length ( $L < L_c = D/k$ ), as in the present case at least in the dark, the relaxation is expected to take the form of a simple exponential, and its time constant  $(\tau)$  can be related to the oxygen surface exchange coefficient,  $k_{\rm chem}$ :

$$\frac{\ln I(t) - \ln I(0)}{\ln I(\infty) - \ln I(0)} = 1 - e^{-t/\tau}$$
(4)

$$k_{chem} = \frac{L}{\tau} \tag{S}$$

where I(t) represents the transmitted intensity at time t, with I(0) and  $I(\infty)$  representing the steady-state transmitted intensity before and after the relaxation, respectively. The relaxations observed in this study could generally be described by eqs 4 and 5, whether induced by a pO<sub>2</sub> step or a UV step, or a pO2 step under simultaneous constant UV illumination. We note that our measurement time resolution is on the order of ~1 s in the current optical data acquisition program, and very fast responses, if present, are not captured. The time constants and k values of relaxations resulting from the two stimuli are plotted in Figure 2a-c, focusing primarily on STF7. Although

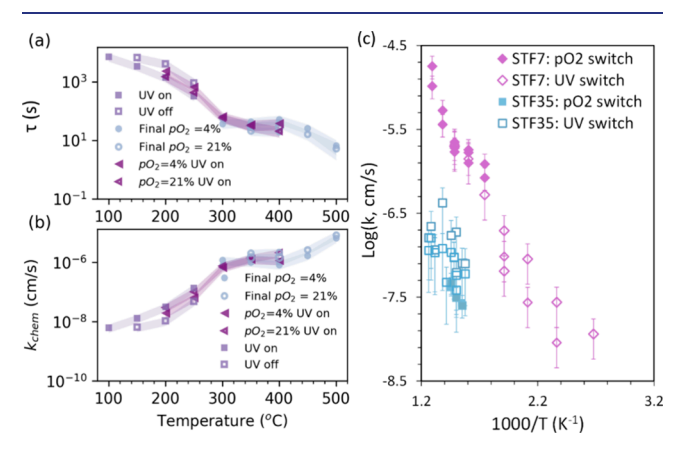


Figure 2. (a) Time constants and (b)  $k_{\text{chem}}$  values of the optical relaxations induced by UV- and/or pO2 steps for a ~440 nm STF7 film on sapphire. Final pO2 of 4% indicates a step change from 21% to 4%, while a final pO<sub>2</sub> of 21% indicates a change from 4% to 21%. Triangles represent a pO2 change during constant UV illumination. UV on/off indicates the values acquired in response to initiation/ discontinuation of the UV light with no change in the ambient gas atmosphere. (c) Comparison of  $k_{\rm chem}$  values obtained by pO $_2$  switching (21%/4% O $_2$ ) in the dark and UV switching (on/off) in 0.21 atm O2 for STF7 and STF35 films across different runs.

the UV-induced relaxations are observable down to a lower temperature range than the pO2-induced relaxations, the time constants appear to be in good agreement on the Arrhenius plot, taking into account the known exponential dependence of  $k_{\rm chem}$  on temperature. The good agreement between the two methods is suggestive of an oxygen-surface-exchange-limited kinetic process when the UV light is turned on or off. Figure 2c compares STF7 and STF35 k values resulting from pO<sub>2</sub>switching and UV-switching, showing similar behavior. The much smaller magnitude of UV-induced optical relaxations for STF35 yields higher uncertainties in k values, which, within error, significantly overlap with  $pO_2$ -induced k values. (The lower  $k_{\text{chem}}$  values for STF35 vs STF7 films were observed

across multiple replicate samples and may be caused by different surface chemistry, e.g., enhanced Sr segregation. The slightly different thicknesses of STF7 vs STF35 are not thought to be responsible, since the STF7 k values were found to be independent of thickness; see Figure S3.)

**3.3. Blocked Surface Studies.** In order to further examine the possibility for an oxygen surface exchange-limited process, we tested samples where the surface was intentionally blocked from exchanging oxygen, but where UV light could still reach the film at the same intensity. In the first example, we coated a STF35 film with ~15 nm amorphous Al<sub>2</sub>O<sub>3</sub> using atomic-layer deposition. (PLD was not suitable for forming a blocking Al<sub>2</sub>O<sub>3</sub> coating due to residual pinholes/pores that permit gas diffusion.) As long as the measurement temperature was kept sufficiently low (T < 400 °C) to keep the Al<sub>2</sub>O<sub>3</sub> layer intact and blocking, no UV- or pO2-induced changes were observed in the visible light transmission. At higher temperature measurements (T > 400 °C), the Al<sub>2</sub>O<sub>3</sub> layer appeared to become nonblocking, possibly due to morphological changes with crystallization-induced densification of the Al<sub>2</sub>O<sub>3</sub> layer, or possibly arising from mismatched thermal expansion with the underlying film. In this case, both pO2 and UV induced optical relaxations could be observed. In the second example, we tested a room-temperature-grown, amorphous STF7 film. As shown in prior work with pO2 switching only, amorphous STF films do not exhibit optical relaxations or apparent oxygen exchange until they are heated sufficiently to induce crystallization; after crystallization, the k values are typically very high, and the optical relaxations are observable and rapid.<sup>21,24</sup> In the present study, the amorphous film similarly did not exhibit visible optical responses to UV illumination until it crystallized. These findings with the capping layer, summarized in Figure 3, and amorphous-to-crystalline films, are again supportive of similar oxygen exchange processes taking place by UV on/off switching or pO<sub>2</sub> switching. Further they suggest that internal redistribution of oxygen in the film (without exchange with the gas phase), or electronic excitation effects only, are not dominating the optical responses observed in this work.

3.4. Impact of UV on pO<sub>2</sub>-Driven Oxygen Exchange **Kinetics.** Although our results indicate that UV exposure switching alone appears sufficient to induce oxygen incorporation and release in the films (as indicated by the optical relaxations at 2.8 eV, their time constants, and their disappearance when surface oxygen blocking layers are added), we also wished to examine the impact of simultaneous UV exposure on pO2-driven oxygen exchange kinetics. In prior work on dilute Fe-doped SrTiO<sub>3</sub> single crystals, UV exposure was reported to increase the rate of pO2 step-driven oxygen incorporation,<sup>7,15</sup> attributed to the role of photogenerated conduction band electrons in the rate-determining step, while oxygen evolution kinetics were unchanged under UV illumination. In our study, we found different results for the nondilute films, as shown in Figures 4 and 2a,b, and Figure S3. First, we observed that pO2-driven optical relaxations could be measured to much lower temperatures when UV light was incident on the film; in other words, the magnitude of the optical changes was larger in the lower temperature range when illuminated, suggestive of larger pO2-driven changes in oxygen content in the films compared to when the UV light is not present and a shifting of the steady-state defect equilibria by the UV light to effectively higher oxygen chemical potentials. On the other hand, there was no significant change

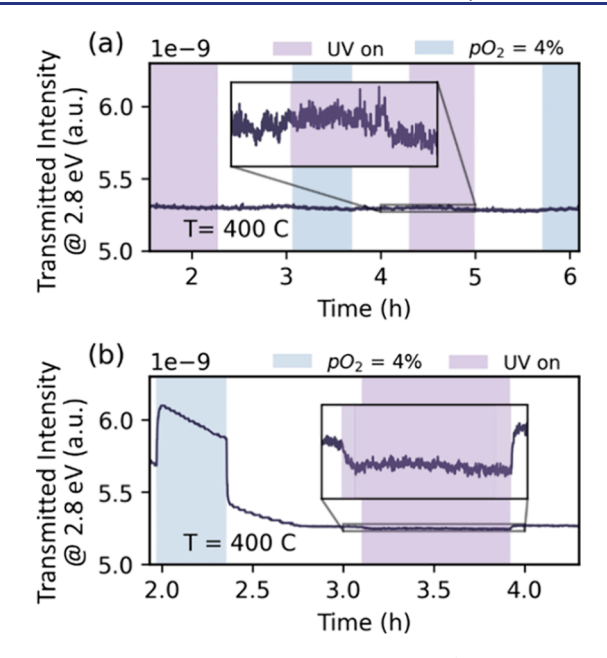


Figure 3. Changes in transmitted light intensity (photocurrent in A registered by the photodetector at  ${\sim}442~\rm nm)$  in response to steps in pO $_2$  of the surrounding gas atmosphere (blue) and to changes in UV illumination (365 nm) for  ${\sim}200~\rm nm$ -thick STF35 samples with (a) an amorphous alumina-coated surface to block oxygen surface exchange and (b) a pristine (unblocked) surface. Final pO $_2$  of 4% represents a change from 21% O $_2$  to 4% O $_2$ . UV on represents a change from dark conditions (no UV illumination) to light conditions (UV illumination).The blocked surface (a) shows no response to changes in pO $_2$  or illumination.

in the *kinetics*; the time constants and their temperature dependence for the  $pO_2$  step-induced relaxations were not affected by the UV light being constantly on vs off. Similarly, in the earlier results shown in Figures 1 and 2, the time constants for UV-induced optical relaxations were similar when turning the light on (relaxation in the UV light) vs turning the light off (relaxation in the dark).

**3.5. Composition Effects.** The baseline composition of a mixed ionic/electronic conductor is expected to play a role in the magnitude and kinetics of its photoionic response. Understanding compositional trends eventually may provide guidelines for engineering materials with sensitive photoionic responses. In this case, prior studies have focused on SrTiO<sub>3</sub> with very dilute Fe impurities or with very dilute Ti vacancies, each of which serve as acceptors that push the system p-type under relatively oxygen-rich conditions. In the present work, we examined nondilute cases with higher Fe concentrations. Increasing the Fe content raises the baseline hole and oxygen vacancy concentrations in the material and its baseline p-type conductivity under the oxygen-rich conditions of this study. In this study, the optimal responses in terms of UV-induced optical relaxation magnitude occurred for x = 0.07 in  $SrTi_{1-x}Fe_xO_{3-x/2+\delta}$  films (compositions measured: x = 0.01, x = 0.01) = 0.07, and x = 0.35). The smaller UV-driven response for x = 0.35 vs x = 0.07 is apparent when comparing Figure 3b to Figure 1b and Figure 4c to Figure 4d. For x = 0.01 responses were too small to detect, perhaps as a result of the film thickness and lower optical absorption coefficient at 2.8 eV for this Fe concentration. For a given composition, the change in optical absorption coefficient ( $\Delta \alpha$ ) is considered proportional to the change in concentration of the absorbing species (and to

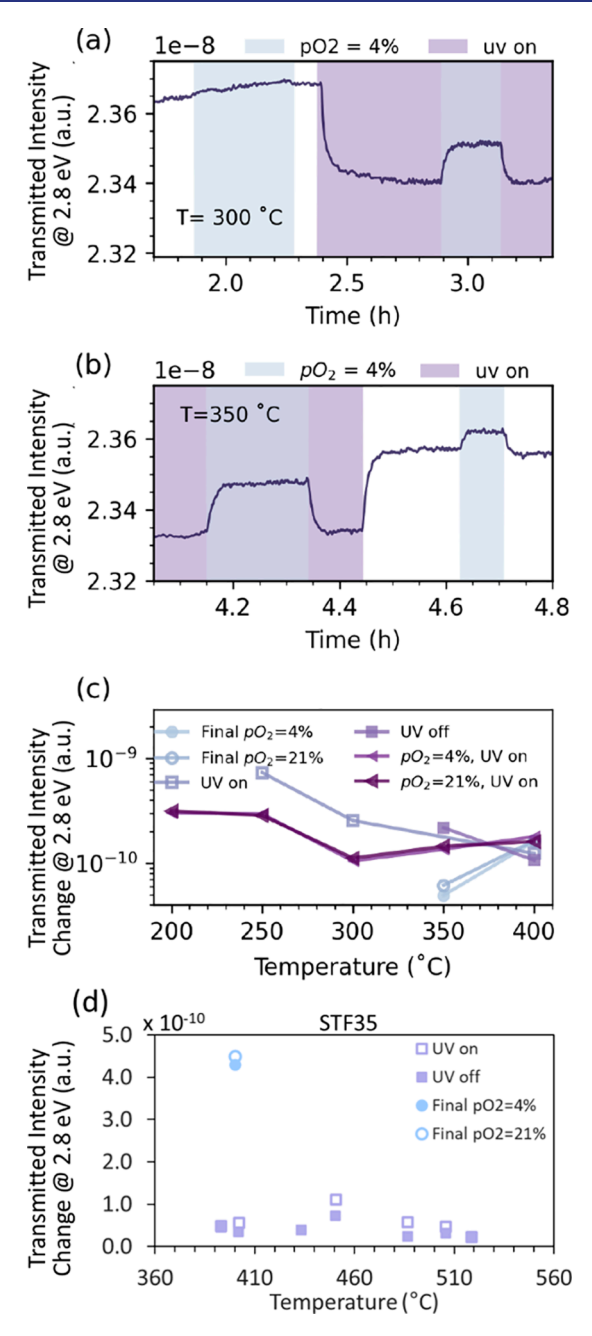


Figure 4. Impact of pO $_2$  steps between 0.21 and 0.04 atm O $_2$  on the visible 2.8 eV transmitted light intensity (photocurrent measured by the photodetector in A), when the UV (3.4 eV) light was on vs off for a  $\sim$  440 nm-thick STF7 film on sapphire. Parts a) and b) show the time-dependent response: visible optical relaxations at 300 and 350 °C, respectively. Part c) summarizes the magnitude of the 2.8 eV transmitted intensity change resulting from pO $_2$  steps down and up in the dark ("Final pO $_2$  = 4%" and "Final pO $_2$  = 21%"), pO $_2$  steps down and up while UV was illuminating the sample ("pO $_2$  = 4%, UV on" and "pO $_2$  = 21%, UV on"), and UV steps on and off in 0.21 atm O $_2$  ("UV on" and "UV off"). For comparison, UV-driven and pO $_2$ -driven transmitted intensity changes at 2.8 eV through a  $\sim$  200 nm-thick STF35 thin film are shown in part d).

 $\Delta\delta$  in STF), with the extinction coefficient  $(\varepsilon_{\delta})$  serving as the proportionality factor, according to the Beer–Lambert law (eq 6); in practice, this relationship holds up well in STF of various Fe concentrations over a limited high pO<sub>2</sub> range, where optical absorption at 2.8 eV appears linearly related to hole

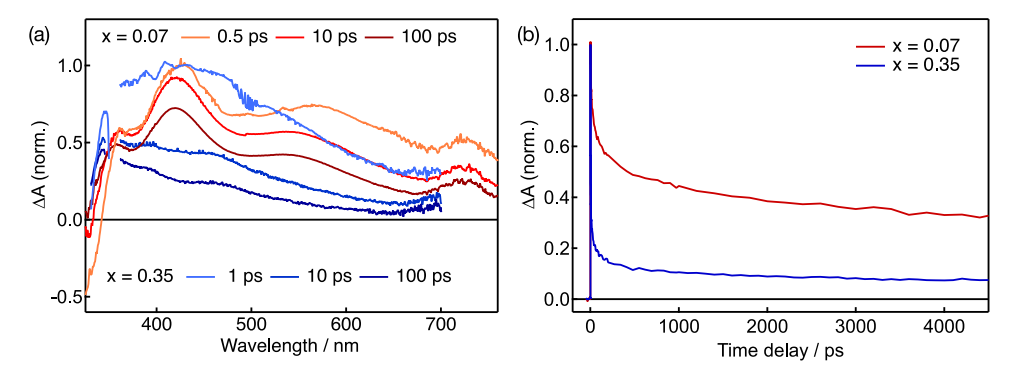


Figure 5. Representative results from ultrafast transient UV/visible spectroscopy for  $SrTi_{1-x}Fe_xO_{3-x/2+\delta}$  thin films with compositions x = 0.07 and x = 0.35 upon photoexcitation at 337 and 355 nm, respectively. (a) Transient spectral traces at three different time delays. The amplitudes are normalized to the maximum amplitude at 425 nm and 0.5 ps. (b) Kinetic traces at 500 nm. The amplitudes are normalized to the maximum.

concentration and thereby oxygen concentration via electroneutrality. 19

$$\Delta \alpha = \varepsilon_{\delta}(T) \Delta \delta \tag{6}$$

Therefore, under such oxidizing conditions, for a given sample at a given temperature, a larger change in transmitted light intensity is indicative of a larger oxygen concentration change in the film, neglecting reflectance changes. Comparing between samples of different compositions at a particular temperature, if the extinction coefficients are similar and Brouwer regimes the same, then a larger optical response to UV light in STF7 vs STF35 suggests that it exhibits the larger UV-driven oxygen stoichiometry change. A caveat is that the extinction coefficients are likely significantly dependent on the absolute oxygen stoichiometry range.

We have estimated the change in hole and oxygen concentrations under UV illumination using two in situ methods: 1) UV-driven change in transmitted intensity of the films relative to pO<sub>2</sub>-driven transmitted intensity changes and known pO2-dependence of hole concentration changes, and 2) UV-driven, in-plane electrical conductivity relaxation measurements (not shown), assuming a constant mobility. For STF35, from electrical measurements we observe hole concentration increases of  $\sim$ 4  $\times$  10<sup>19</sup> cm<sup>-3</sup> under continuous 3.4 eV UV illumination at ~10 mW/cm<sup>2</sup> on the sample at 400–450 °C and 0.21 atm  $O_2$ , assuming a baseline hole concentration in the range  $3.5-4\times10^{21}$  cm<sup>-3</sup> in accordance with our prior STF35 thin-film defect model. 18 In other words, the increase over the baseline concentration is on the order of  $\sim$ 1%. This quantity corresponds to an increase in oxygen concentration of  $\sim 2 \times 10^{19}$  cm<sup>-3</sup> under UV illumination if the standard simplified electroneutrality condition applies. For STF7, using optical measurements (e.g., Figure 4c), we estimate a UV-driven hole concentration increase of ~15-30% over the dark baseline at 400 °C under the same conditions, which rises at lower temperatures. Note that the baseline hole concentration is expected to be lower in the dark for STF7, so a larger percent change vs STF35 under UV illumination is reasonable. More precise determination of the UV-induced concentration changes in STF7 films can be obtained in the future by electrically establishing the pO<sub>2</sub>dependence of hole concentration in the dark; the power-law exponent is well below 1/4 for STF35 films under these conditions, for example.

To investigate the composition effect further, we conducted ultrafast transient UV/visible spectroscopy for STF7 and

STF35 thin films upon photoexcitation in the UV at room temperature (see Experimental Section for details). The time scale of this experiment (several ns) is too fast for significant oxygen uptake to take place, particularly at room temperature. We are thus probing the initial carrier dynamics after abovegap photoexcitation that leads to excited holes and electrons in the valence and conduction bands, respectively. Figure 5a,b shows representative transient spectra and kinetic traces for STF7 upon excitation at 337 nm, and STF35 upon excitation at 355 nm. (The static spectra are provided in Figure S4 where the shift of the absorption edge energy with respect to composition accounts for the slight difference in excitation wavelength.) The amplitudes of the transient data have been normalized to account for differences in absorption cross section - here we focus on the qualitative comparison between decay time scales and spectral features for the two compositions. At early times after photoexcitation, the spectrum is dominated by a broad excited-state absorption band spanning the entire UV/visible range between 350 and 750 nm with features peaking around 420, 535, and 720 nm for the STF7 sample. These features are blue-shifted by 30-50 nm for the STF7 sample due to changes in the band structure as a result of the different dopant concentration. On the very blue side of the spectrum around ~320 nm a bleach feature can be seen, which is attributed to the depleted ground-state band gap absorption caused by excited carriers in the conduction band. The induced absorption features in the visible may result from transitions from excited carriers trapped in midgap states resulting from the presence of dopants and defects. Previous transient absorption experiments on Cr/La-doped SrTiO3 have assigned the absorption band around 720 nm to the presence of photogenerated holes.<sup>38</sup>

The kinetics (Figure 5b) cannot be satisfactorily fitted by multiexponential functions. However, roughly two decay time scales can be distinguished: few-to-tens of ps and few-ns, both assigned to carrier recombination of trapped charges. Significant induced absorption remains even at the longest time delay of the setup (5 ns) suggesting the presence of long-lived charge carriers. The longest carrier recombination time is expected to be on the  $\mu$ s scale, outside of the measurement window. A comparison of the kinetics for composition x = 0.07 and x = 0.35 shows that much of the spectral amplitude is lost during the first few ps, indicating an efficient charge carrier recombination pathway right after photoexcitation. This is more pronounced for the x = 0.35 sample (75% loss within 20 ps) than for the x = 0.07 sample (25% loss within 20 ps).

While a decisive assignment of the transient bands and kinetics would require more elaborate investigations for other compositions, longer time scales, and in the presence and absence of electron and hole scavengers, we can conclude that the STF35 generally shows faster kinetics and a significantly larger excited carrier loss at early time scales than STF7. This difference may be due to the higher defect concentration in the STF35 (defect sites promoting carrier recombination). In a qualitative picture, the longer the lifetime of the excited carriers (on the ns-us time scale), the larger their steady-state concentration under continuous light irradiation, the larger the changes in the energy levels, and the larger the photoionic effect, in agreement with the results described in the previous section.

# 4. DISCUSSION WITH SUPPORTING COMPUTATIONAL RESULTS

- **4.1. Mechanism.** In principle, visible optical absorption changes under UV illumination could arise from several mechanisms:
  - 1. Excited carrier generation from above-gap UV absorption could modify surface space charge layers, with flattening of electronic carrier profiles leading to a redistribution of ionic species in the near-surface region. We expect this effect, if present, to result in only minor changes in the optical absorption, given the expectation of small or negligible space-charge depths at these relatively high Fe concentrations relative to the film thickness, and therefore only a very small volume of the film participating. Alternatively but by a similar mechanism, since the films are nanocrystalline, light absorption may flatten band bending at grain boundaries, with a similar near-interface redistribution of oxygen content. However, again, one expects negligible spacecharge effects at interfaces such as grain boundaries at this Fe concentration compared to undoped SrTiO<sub>3</sub>. 16 Furthermore, the diffusion distances for oxygen are so short that the attainment of a new steady-state should appear almost instantaneously, in contrast to the observed gradual optical relaxations when the UV light is turned on or off. Epitaxial (grain boundary-free) film studies in the future may be beneficial to completely rule out microstructure contributions.
  - 2. Excited carrier generation will be depth-dependent since UV intensity drops exponentially with depth. Given possibly different diffusion lengths and lifetimes of excited electrons vs holes, the depth-dependent excited carrier generation could result in a different spatial distribution of hot electrons vs holes and therefore development of an electric field. In this case, the electric field could drive redistribution of mobile oxygen as a function of depth within the illuminated sample (an ionic extension of the photo-Dember effect). In the present work, this mechanism is deemed unlikely for two reasons: (a) The film thicknesses were kept intentionally on the order of the UV absorption depth in these compositions; therefore, light intensity is estimated to vary by only a factor of 2-3 from top to bottom of the film. (b) The length of time expected for oxygen to redistribute through the depth of the film is calculated to be faster than the time resolution of the data acquisition, given known oxygen diffusion coefficients at these

- temperatures<sup>39</sup> and the short diffusion distance. The observed time constants were considerably longer (Figure 1a), over 1000 s at the lowest temperatures studied. Further, no optical response was observed when the films were capped with the UV-transparent but O<sub>2</sub>-blocking surface layer, indicating that oxygen exchange with the gas phase is the dominant mechanism, rather than internal solid-phase oxygen redistribution in response to a photovoltage.
- 3. UV illumination might induce or modify asymmetry of the interfacial reaction kinetics for oxygen incorporation vs release at the film surface. However, this effect alone would not be enough to induce photochromism without an electrochemical potential driving force. In this work the relaxation times for UV on vs off and for pO2 down vs up (with vs without background UV illumination) were all consistent with each other. There was no evidence in this work of enhanced oxygen exchange kinetics due to the presence of excess electronic carriers, both for oxygen incorporation and evolution. The result stands in contrast to that of Merkle et al., who observed enhanced oxygen surface incorporation rates (but not evolution rates) under UV illumination on dilute SrTiO<sub>3</sub>:Fe single crystals, <sup>7,15</sup> attributed to a role of conduction band electrons in the rate-determining step. We surmise that, in the present work, the higher baseline hole concentrations, which led to already much higher baseline k values, may have rendered the impact of excess carriers on k less significant; in STF7 we estimated a  $\sim 15-30\%$  increase in hole concentration under illumination at 400 °C (and ~1% for STF35), which may be insufficient to raise k beyond uncertainty in the intermediate temperature range. On the other hand, the relative concentration change of minority carriers (electrons) under illumination is more significant, and if this shift lowers the activation energy for surface oxygen exchange at all, the impact on k might be more noticeable at lower temperatures than those studied. Alternatively, the diminished surface space charge expected in the nondilute compositions vs SrTiO<sub>3</sub>, or differences in surface chemistry with increasing Fe concentration, might play a role. Regardless, the observed photochromism cannot be attributed to UV-induced changes in surface exchange kinetics in the present work.
- 4. UV illumination can increase the oxygen (quasi-)chemical potential in the film. While, in principle, UV-generation of gas-phase ozone near the film surface from the ambient O2 might cause an increase in oxygen content in the film due to the induced electrochemical potential gradient across the interface, the 365 nm light used in the present work is not energetic enough to cause such an effect. (Ozone is only generated at considerably lower wavelengths.) Instead, we consider that oxygen chemical potential may increase in the film under illumination-induced excess carrier generation due to the uneven influence of electron vs hole quasi-Fermi level shifts in the bulk of the material. In STF in the dark under relatively oxidizing conditions, the Fermi level is expected to be near the top of the valence band with much higher baseline hole concentrations than electron concentrations.<sup>19</sup> Generation of electron-hole pairs under UV illumination therefore causes a bigger relative

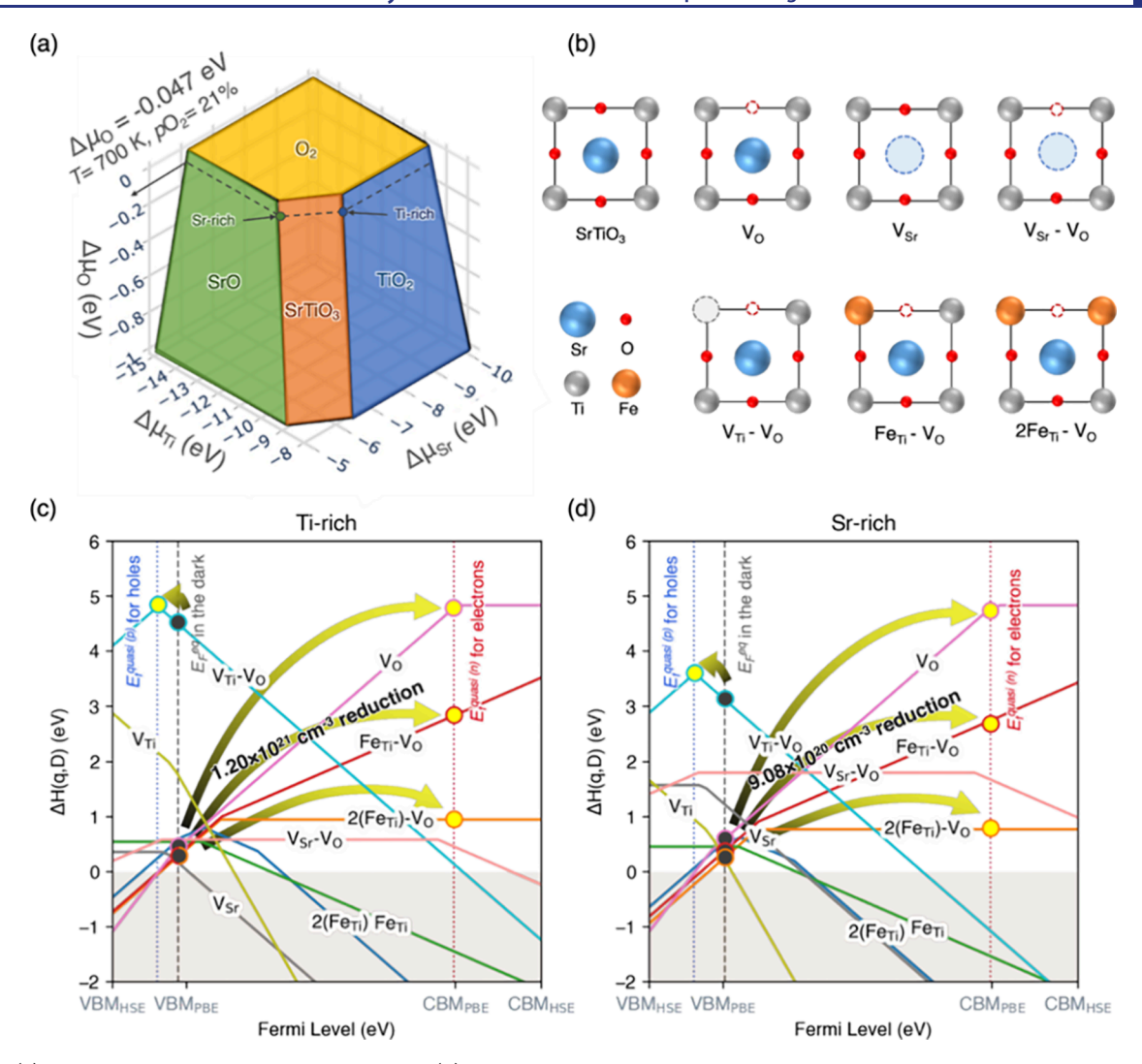


Figure 6. (a) The chemical stability diagram of  $SrTiO_3$ . (b) 2D illustration of key defect configurations. The blue, gray, orange, and red colored atoms represent Sr, Ti, Fe, and O atoms, respectively. Defect formation energy plots under (c) Ti-rich and (d) Sr-rich conditions. The equilibrium Fermi energies (in the dark) are represented in the dashed gray lines, while potential quasi-Fermi energies for electrons (n) and holes (p) are marked as red and blue colored dotted lines, respectively.

change in minority electron concentrations than in majority hole concentrations. For a complementary approach, we consider application of a steady-state ratebased model developed for semiconductor growth under light by Alberi and Scarpulla.40 Charged defect concentrations depend exponentionally on their formation enthalpies, which in turn depend on the Fermi level. Assuming the charged defect is dynamically exchanging electrons or holes with the conduction band or valence band, the rate of capture and emission is likely faster if that defect's charge transition level is closer to the respective band edge. Under light excitation, rather than all defect concentrations equilibrating to a single equilibrium Fermi level, donor defects that exchange carriers with the conduction bands equilibrate with the n-type quasi-Fermi level, while acceptor defects that exchange with the valence bands equilibrate with the p-type quasi-Fermi level. Therefore, for a typical p-type conductor with compensating positive ionic defects, the compensating defect's concentration is expected to be more closely dependent on the electron quasi Fermi level. In this case the

positively charged compensating ionic defect formation energy increases as the electron quasi-Fermi level increases, leading to a decrease of concentration under increasing excited carrier populations. A first-principles model suggesting this same trend has been developed for dilute Fe-doped SrTiO<sub>3</sub> by Irving et al.<sup>41</sup> In what follows, we describe our simulations for a higher Fe concentrations and permitting formation of several key defect complexes.

**4.2. First-Principles Simulations of Defect Populations Under Steady State Excitation.** To explore possible changes to defect equilibria under steady-state above bandgap excitation, we carried out first-principles simulations of Ferelated defects, native defects, and defect complexes in 10%-Fe doped SrTiO<sub>3</sub>. On the basis of changes induced to electron and hole quasi-Fermi levels, we investigated how steady state excess carrier populations resulting from light excitation modify defect equilibria by suppressing populations of compensating donor defects.

Especially at nondilute Fe doping concentrations, defect—defect interactions between Fe substitutional defects and native defects such as  $Fe_{Ti}$ - $V_O$  and  $Fe_{Ti}$ - $V_O$ - $Fe_{Ti}$  govern defect

equilibria, carrier concentrations, and stoichiometry. Kim et al. used cluster expansion models to show that the 2(Fe<sub>Ti</sub>)-V<sub>O</sub> chain structure is the most favorable motif found in STF, with other complexes such as  $2(Fe_{Ti})$ ,  $Fe_{Ti}$ - $V_O$ , and  $V_O$ - $V_{Ti}$  also present. 42 By incorporating these defect complexes within our dilute limit framework, we elucidate the effect of various defect-defect interactions, bridging the gap between the theoretical simplicity of the dilute limit and the complexity of alloyed materials. The full set of defect complexes considered is shown in Figure S5.

Figure 6 shows the results of the defect analysis (defect diagrams encompassing all defects, including those with higher energy, are provided in Figure S6). We consider thermodynamic environments corresponding to partial oxygen pressure  $P(O_2)$  at 0.21 bar (equivalent to ambient conditions) with two limits of Ti-rich (Sr-poor) and Sr-rich (Ti-poor) conditions (see Table S7), as shown in Figure 6a. Figure 6b shows the suite of defect complexes considered. To incorporate a wide range of defect-defect ordering, we included various Fe defect complexes that were previously predicted (Fe<sub>Ti</sub>-V<sub>O</sub>, <sup>43</sup> 2(Fe<sub>Ti</sub>)- $V_0^{42}$ ) or designed (2(Fe<sub>Ti</sub>)). Figure 6c,d show the calculated defect formation energies in equilibrium under Ti-rich and Srrich conditions, respectively.

As illustrated in Figure 6c,d, the positions of equilibrium  $E_{\text{Fermi}}$  are predicted within the "defect tents", where lowest energy defects primarily fix the  $E_{\rm Fermi}$  and carrier concentrations of the material. Under dark conditions, the most energetically favorable native defects vary depending on the chemical environments: in Ti-rich conditions, Sr and oxygen vacancies (V<sub>Sr</sub> and V<sub>O</sub>) predominate near the equilibrium  $E_{\text{Fermi}}$ , while in Sr-rich conditions, Ti and oxygen vacancies  $\left(V_{Ti} \text{ and } V_{O}\right)$  are most favorable among all native defects. Vacancies  $V_{Ti}$  and  $V_{Sr}$  have low formation energy, the latter of which enables facile formation of Fe substitutionals. Among Fe-related defects, Fe and  $V_O$  complexes  $((2(Fe_{Ti})-V_O)^{2+})$  and (Fe<sub>Ti</sub>-V<sub>O</sub>)<sup>2+</sup>) exhibit the lowest formation energies around the equilibrium  $E_{\text{Fermi}}$ , as a result of the constraint of [Fe] = 10%. These five dominant defects  $(V_{Sr}, V_{Ti}, V_O, (2(Fe_{Ti})-V_O)^{2+})$  and  $({\rm Fe_{Ti}}{-}{\rm V_O})^{2+})$  pin the equilibrium  $E_{\rm Fermi}$  below mid gap, resulting in p-type characteristics of STF all over chemical potential conditions, aligning with experiments. Interestingly, under our high  $P(O_2)$  conditions, these Fe and  $V_O$  complexes  $[(2(Fe_{Ti})-V_O)^{2+}]$  and  $(Fe_{Ti}-V_O)^{2+}$  are more favorable than other Fe complexes, such as  $(2Fe_{Ti})$  and  $(Fe_{Ti})$ , contributing to oxygen deficiency. The total concentrations of oxygen vacancies derived from all Fe and Vo complexes range from  $1.20 \times 10^{21}$  cm<sup>-3</sup> (2.4%) in Ti-rich and  $9.08 \times 10^{20}$  cm<sup>-3</sup> (1.8%) in Sr-rich conditions at 700 K. This predicted oxygen deficiency aligns closely with the findings from experiments of bulk STF. 17,3

Dominant defects that give rise to p-type behavior are V<sub>Sr</sub><sup>2-</sup> and  $V_{Ti}^{4-}$ . The dominant compensating donors are (2(Fe<sub>Ti</sub>)- $(V_O)^{2+}$ ,  $(Fe_{Ti}V_O)^{2+}$  and  $(V_O)^{2+}$ . This observation suggests a mechanism for the incorporation of oxygen under illumination. Under illumination, the introduction of excess hole and electron carriers causes the equilibrium Fermi energy to split into n-type and p-type quasi-Fermi levels, nQFL and pQFL respectively, 41,44 represented by blue and red dotted lines in Figure 6c,d. Under steady state excitation, acceptor defects such as  $(V_{Ti}-V_O)^{2-}$  as well as native cation vacancies largely equilibrate with pQFL, while compensating donor defects  $(2(Fe_{Ti})-V_O)^{2+}$ ,  $(Fe_{Ti}-V_O)^{2+}$  and  $V_O^{2+}$  largely equilibrate with nQFL. The compensating defects are most affected by the significant increase in photogenerated minority carriers as shown by the arrows in Figure 6c,d.

As shown in Figure 6c, under Ti-rich conditions, the concentrations of compensating  $(2(Fe_{Ti})-V_O)^{2+}$ ,  $(Fe_{Ti}-V_O)^{2+}$  and  $V_O^{2+}$  decrease from  $5.24\times10^{20}$ ,  $6.03\times10^{20}$  and  $3.82\times10^{19}~cm^{-3}$  to merely  $3.15\times10^{-11}$ ,  $3.62\times10^{-11}$  and  $2.29\times10^{-11}$ 10<sup>-12</sup> cm<sup>-3</sup>, respectively, indicating the entire annihilation of these defects in the bulk under illumination. Under Sr-rich conditions (Figure 6d), the concentration of  $(2(Fe_{Ti})-V_O)^{2+}$ ,  $({\rm Fe_{Ti}} {\rm V_O})^{2+}$  and  ${\rm V_O}^{2+}$  are also reduced from 7.12  $\times$  10<sup>20</sup>, 1.87  $\times$  10<sup>20</sup> and 2.72  $\times$  10<sup>18</sup> cm<sup>-3</sup> to merely 6.00  $\times$  10<sup>-10</sup>, 1.58  $\times$  $10^{-10}$  and  $2.29 \times 10^{-12} \text{ cm}^{-3}$ , respectively. The notable decrease in overall Vo concentrations is attributed to the oxidation processes where  $(2(Fe_{Ti})-V_O)^{2+}$  is oxidized to  $Fe_{Ti}-O_O-Fe_{Ti}$  defects in Ti-rich conditions, and  $(Fe_{Ti}-V_O)^{2+}$  is oxidized to isolated Fe<sub>Ti</sub>-O<sub>O</sub> defects in Sr-rich conditions. We note that our study assumes only oxygen is mobile enough to reach quasi-equilibrium under the illumination and cation defects remain unchanged except for the incorporation of oxygen into the vacancy sites. These substantial reductions in V<sub>O</sub> concentrations resulting from the annihilation of Fe<sub>Ti</sub>-V<sub>O</sub> and Vo indicate a significant influx of oxygen into the bulk STF under illumination.

These results are consistent with our experimental observations, and earlier experimental and theoretical conclusions, indicating increased oxygen incorporation in bulk SrTiO<sub>3</sub> under illumination. Specifically, Wu et al.<sup>41</sup> suggested, from simulations, that UV illumination triggers the dissociation of the (Fe<sub>Ti</sub>-V<sub>O</sub>) complex in dilute-doped SrTiO<sub>3</sub>, leading to a huge reduction in V<sub>O</sub> concentration, and Viernstein et al.<sup>12</sup> proposed oxygen is incorporated into dilute-doped SrTiO<sub>3</sub> single crystals upon illumination, leading to a decrease in V<sub>O</sub> concentrations. However, the significant concentrations of Fe and the comprehensive array of defect clusters examined in this study uncover further patterns. First, the effects of light excitation on oxygen stoichiometry are somewhat mitigated in STF by the presence of highly energetically stable and charge neutral complex 2(Fe<sub>Ti</sub>)-Vo whose formation energy and concentration is independent of the Fermi energy. Similarly, the favorable V<sub>Sr</sub>-V<sub>O</sub> Shottky defect serves as another low energy, charge neutral reservoir for VO that is unaffected by excess carriers. Finally, as a result of the increased formation energy of the (Fe<sub>Ti</sub>-V<sub>O</sub>) and (2(Fe<sub>Ti</sub>)-V<sub>O</sub>) complexes, we find that light excitation may also induce a thermodynamic driving force for reduction of Fe<sup>4+</sup> concentration.

# 5. CONCLUSIONS

Our results demonstrate that steady-state, low irradiance illumination above the band gap can induce oxidation of nondilute STF films via oxygen incorporation from the gas phase, and that the behavior is completely reversible once the UV light is removed. The behavior is consistent with oxygen stoichiometry changes induced by gas-phase oxygen partial pressure changes, with similar time constants. From this similarity, we surmise that the kinetics are oxygen-surfaceexchange limited, reasonable given the low film thickness relative to the absorption depth and critical length for the onset of diffusion-limited behavior. The work agrees qualitatively with prior reports of UV-induced photochromism in single crystal SrTiO3 attributed to oxygen incorporation, but differs in that the prior work was concerned with dilute defects, sample thickness well above the absorption depth, and often diffusion-limited kinetics. The thin film geometry of the

present work instead enabled a focus on the oxygen surface exchange kinetics and insight into the mechanism of the optical response-minimizing ionic photo-Dember and space charge contributions. No kinetic enhancement in surface exchange coefficients was observed by excess carrier generation, in contrast to prior work on dilute-doped SrTiO<sub>3</sub>; in this case, the high baseline hole concentration and/or possible absence of space-charge effects due to the nondilute Fe content may play a role. The larger apparent oxygen stoichiometry change in STF7 vs STF35 correlated with longer excited states observed in transient ultrafast spectroscopy at time scales where O exchange was not taking place; this result may suggest a relationship between excited carrier lifetime and magnitude of the photoionic stoichiometry response. First-principles simulations showed higher formation enthalpies for ionized oxygen vacancies and charged defect associates containing oxygen vacancies in the excited state, when the Fermi level splits; this effect provides a plausible driving force for the experimentally observed oxygen fluxes under above-gap illumination. Based on the findings, we hypothesize that materials with long excited carrier lifetimes and highly charged defects or defect complexes may support large above-gap illumination-driven stoichiometry changes. In-depth, quantitative investigations into the impact of varying Fe concentration on a) optically measured stoichiometry changes and kinetic responses to UV illumination and b) simulated stoichiometry changes for such nondilute systems remain potential avenues for future work. The ability to induce oxygen fluxes and stoichiometry changes by significant amounts in real-world, nondilute compositions is promising for a new generation of photoionic devices leveraging wireless control of defect profiles with high spatial and temporal resolution.

# ASSOCIATED CONTENT

# Supporting Information

The Supporting Information is available free of charge at https://pubs.acs.org/doi/10.1021/jacs.4c05764.

Film structural/chemical characterization by X-ray diffraction and Rutherford backscattering spectrometry; thickness dependence of k values for STF7 replicates in response to pO<sub>2</sub> changes in the dark, UV switches, and pO<sub>2</sub> changes during illumination; static absorption spectra for STF7 and STF35; and further outcomes of the first-principles simulations by density functional theory, including illustration of defect configurations, defect formation energies of the full set of defects simulated, and chemical potential shifts for each anion and cation at the limiting conditions studied (PDF)

# AUTHOR INFORMATION

#### **Corresponding Author**

Nicola H. Perry — Department of Materials Science & Engineering, University of Illinois, Urbana—Champaign, Urbana, Illinois 61801, United States; Materials Research Laboratory, Urbana, Illinois 61801, United States; orcid.org/0000-0002-7207-2113; Email: nhperry@illinois.edu

# **Authors**

Emily J. Skiba – Department of Materials Science & Engineering, University of Illinois, Urbana–Champaign, Urbana, Illinois 61801, United States; Materials Research

Laboratory, Urbana, Illinois 61801, United States; orcid.org/0000-0002-9066-6492

Haley B. Buckner — Department of Materials Science & Engineering, University of Illinois, Urbana—Champaign, Urbana, Illinois 61801, United States; Materials Research Laboratory, Urbana, Illinois 61801, United States

Channyung Lee – Department of Mechanical Science & Engineering, University of Illinois, Urbana–Champaign, Urbana, Illinois 61801, United States

Grace McKnight — Department of Mechanical Science & Engineering, University of Illinois, Urbana—Champaign, Urbana, Illinois 61801, United States

Rachel F. Wallick – Department of Chemistry, University of Illinois, Urbana–Champaign, Urbana, Illinois 61801, United States; orcid.org/0000-0002-7548-4850

Renske van der Veen – Department of Chemistry, University of Illinois, Urbana–Champaign, Urbana, Illinois 61801, United States; Helmholtz-Zentrum Berlin für Materialien und Energie (HZB), Berlin 14109, Germany; orcid.org/0000-0003-0584-4045

Elif Ertekin — Materials Research Laboratory, Urbana, Illinois 61801, United States; Department of Mechanical Science & Engineering, University of Illinois, Urbana—Champaign, Urbana, Illinois 61801, United States; orcid.org/0000-0002-7816-1803

Complete contact information is available at: https://pubs.acs.org/10.1021/jacs.4c05764

#### **Author Contributions**

<sup>≈</sup>E.J.S., H.B.B., C.L., and G.M. have equal contribution.

The authors declare no competing financial interest.

#### ACKNOWLEDGMENTS

This work was supported primarily by the Illinois Materials Research Science and Engineering Center (I-MRSEC) under NSF Award Number DMR-2309037. Experimental characterization was carried out in part in the Materials Research Laboratory Central Research Facilities, University of Illinois. The authors acknowledge the use of facilities and instrumentation supported by NSF through the University of Illinois Urbana-Champaign Materials Research Science and Engineering Center DMR-2309037. RMvdV and RFW were partially supported by a Packard Fellowship in Science and Engineering from the David and Lucile Packard Foundation. EE and CL acknowledge partial support provided by the Air Force Office of Scientific Research under Award No. FA9550-21-1-0353 (Program Manager: Dr. Ali Sayir). This work used PSC Bridges-2 at the Pittsburgh Supercomputing Center through allocation MAT220011 from the Advanced Cyberinfrastructure Coordination Ecosystem: Services & Support (ACCESS) program, which is supported by National Science Foundation grants #2138259, #2138286, #2138307, #2137603, and #2138296.

## REFERENCES

- (1) (a) Moss, T. S.; Burrell, G. J.; Ellis, B. Semiconductor optoelectronics; Butterworth-Heinemann, 2013. (b) Piprek, J. Semiconductor optoelectronic devices: introduction to physics and simulation; Elsevier, 2013.
- (2) Siebenhofer, M.; Viernstein, A.; Morgenbesser, M.; Fleig, J.; Kubicek, M. Photoinduced electronic and ionic effects in strontium titanate. *Mater. Adv.* **2021**, *2* (23), 7583–7619.

- (3) Knauth, P.; Tuller, H. L. Solid-state ionics: roots, status, and future prospects. J. Am. Ceram. Soc. 2002, 85 (7), 1654–1680.
- (4) Maier, J. Physical chemistry of ionic materials: ions and electrons in solids; John Wiley & Sons, 2023.
- (5) Smyth, D. M. The defect chemistry of metal oxides; Oxford University Press, 2000.
- (6) Tuller, H. L.; Bishop, S. R. Point defects in oxides: tailoring materials through defect engineering. *Annu. Rev. Mater. Res.* **2011**, *41*, 369–398.
- (7) Merkle, R.; De Souza, R. A.; Maier, J. Optically Tuning the Rate of Stoichiometry Changes: Surface-Controlled Oxygen Incorporation into Oxides under UV Irradiation. *Angew. Chem., Int. Ed.* **2001**, *40* (11), 2126–2129.
- (8) Lee, C.-W.; Schleife, A. Hot-electron-mediated ion diffusion in semiconductors for ion-beam nanostructuring. *Nano Lett.* **2019**, *19* (6), 3939–3947.
- (9) Gordiz, K.; Muy, S.; Zeier, W. G.; Shao-Horn, Y.; Henry, A. Enhancement of ion diffusion by targeted phonon excitation. *Cell Rep. Phys. Sci.* **2021**, 2 (5), No. 100431.
- (10) Wagner, C. Equations for transport in solid oxides and sulfides of transition metals. *Prog. Solid State Chem.* **1975**, *10*, 3–16.
- (11) Kim, G. Y.; Senocrate, A.; Yang, T.-Y.; Gregori, G.; Grätzel, M.; Maier, J. Large tunable photoeffect on ion conduction in halide perovskites and implications for photodecomposition. *Nat. Mater.* **2018**, *17* (5), 445–449.
- (12) Viernstein, A.; Kubicek, M.; Morgenbesser, M.; Walch, G.; Brunauer, G. C.; Fleig, J. High-Temperature Photochromism of FeDoped SrTiO3 Caused by UV-Induced Bulk Stoichiometry Changes. *Adv. Funct. Mater.* **2019**, 29 (23), No. 1900196.
- (13) Viernstein, A.; Kubicek, M.; Morgenbesser, M.; Huber, T. M.; Ellmeyer, E.; Siebenhofer, M.; Vaz, C. A. F.; Fleig, J. Mechanism of photo-ionic stoichiometry changes in SrTiO3. *Solid State Ionics* **2022**, 383, No. 115992.
- (14) Viernstein, A.; Kubicek, M.; Morgenbesser, M.; Huber, T. M.; Siebenhofer, M.; Fleig, J. How UV light lowers the conductivity of SrTiO3 by photochemical water splitting at elevated temperature. *Materials Advances* **2022**, *3* (6), 2800–2809.
- (15) Merkle, R.; Maier, J. Oxygen incorporation into Fe-doped SrTiO3: Mechanistic interpretation of the surface reaction. *Phys. Chem. Chem. Phys.* **2002**, *4* (17), 4140–4148.
- (16) Jurado, J. R.; Colomer, M. T.; Frade, J. R. Impedance spectroscopy of Sr0.97Ti1-xFexO3 $-\delta$  materials with moderate Fecontents. *Solid State Ionics* **2001**, 143 (2), 251-257.
- (17) Kuhn, M.; Kim, J. J.; Bishop, S. R.; Tuller, H. L. Oxygen Nonstoichiometry and Defect Chemistry of Perovskite-Structured BaxSr1-xTi1-yFeyO3-y/2+ $\delta$  Solid Solutions. *Chem. Mater.* **2013**, 25 (15), 2970–2975.
- (18) Perry, N. H.; Pergolesi, D.; Bishop, S. R.; Tuller, H. L. Defect chemistry and surface oxygen exchange kinetics of La-doped  $Sr(Ti,Fe)O3-\alpha$  in oxygen-rich atmospheres. *Solid State Ionics* **2015**, 273, 18–24
- (19) Perry, N. H.; Kim, N.; Ertekin, E.; Tuller, H. L. Origins and Control of Optical Absorption in a Nondilute Oxide Solid Solution: Sr(Ti,Fe)O3-x Perovskite Case Study. *Chem. Mater.* **2019**, *31* (3), 1030–1041.
- (20) Perry, N. H.; Kim, J. J.; Bishop, S. R.; Tuller, H. L. Strongly coupled thermal and chemical expansion in the perovskite oxide system  $Sr(Ti,Fe)O3-\alpha$ . Journal of Materials Chemistry A **2015**, 3 (7), 3602–3611.
- (21) Chen, T.; Harrington, G. F.; Sasaki, K.; Perry, N. H. Impact of microstructure and crystallinity on surface exchange kinetics of strontium titanium iron oxide perovskite by in situ optical transmission relaxation approach. *Journal of Materials Chemistry A* **2017**, 5 (44), 23006–23019.
- (22) Buckner, H. B.; Perry, N. H. In Situ Optical Absorption Studies of Point Defect Kinetics and Thermodynamics in Oxide Thin Films. *Advanced Materials Interfaces* **2019**, *6* (15), No. 1900496.
- (23) Chen, T.; Harrington, G. F.; Masood, J.; Sasaki, K.; Perry, N. H. Emergence of Rapid Oxygen Surface Exchange Kinetics during in Situ

- Crystallization of Mixed Conducting Thin Film Oxides. ACS Appl. Mater. Interfaces 2019, 11 (9), 9102-9116.
- (24) Skiba, E. J.; Chen, T.; Perry, N. H. Simultaneous Electrical, Electrochemical, and Optical Relaxation Measurements of Oxygen Surface Exchange Coefficients: Sr(Ti,Fe)O3-d Film Crystallization Case Study. ACS Appl. Mater. Interfaces 2020, 12 (43), 48614–48630.
- (25) (a) Hohenberg, P.; Kohn, W. Inhomogeneous Electron Gas. *Phys. Rev.* **1964**, *136* (3B), B864–B871. (b) Kohn, W.; Sham, L. J. Self-Consistent Equations Including Exchange and Correlation Effects. *Phys. Rev.* **1965**, *140* (4A), A1133–A1138.
- (26) (a) Blöchl, P. E. Projector augmented-wave method. *Phys. Rev. B* **1994**, *50* (24), 17953–17979. (b) Kresse, G.; Joubert, D. From ultrasoft pseudopotentials to the projector augmented-wave method. *Phys. Rev. B* **1999**, *59* (3), 1758–1775.
- (27) (a) Kresse, G.; Furthmüller, J. Efficient iterative schemes for ab initio total-energy calculations using a plane-wave basis set. *Phys. Rev. B* **1996**, *54* (16), 11169–11186. (b) Kresse, G.; Furthmüller, J. Efficiency of ab-initio total energy calculations for metals and semiconductors using a plane-wave basis set. *Comput. Mater. Sci.* **1996**, *6* (1), 15–50.
- (28) Perdew, J. P.; Burke, K.; Ernzerhof, M. Generalized Gradient Approximation Made Simple. *Phys. Rev. Lett.* **1996**, 77 (18), 3865–3868.
- (29) Perdew, J. P.; Wang, Y. Accurate and simple analytic representation of the electron-gas correlation energy. *Phys. Rev. B* **1992**, 45 (23), 13244–13249.
- (30) Anisimov, V. I.; Zaanen, J.; Andersen, O. K. Band theory and Mott insulators: Hubbard U instead of Stoner I. *Phys. Rev. B* **1991**, *44* (3), 943–954.
- (31) Stevanović, V.; Lany, S.; Zhang, X.; Zunger, A. Correcting density functional theory for accurate predictions of compound enthalpies of formation: Fitted elemental-phase reference energies. *Phys. Rev. B* **2012**, *85* (11), 115104.
- (32) Monkhorst, H. J.; Pack, J. D. Special points for Brillouin-zone integrations. *Phys. Rev. B* **1976**, *13* (12), 5188–5192.
- (33) (a) Freysoldt, C.; Grabowski, B.; Hickel, T.; Neugebauer, J.; Kresse, G.; Janotti, A.; Van de Walle, C. G. First-principles calculations for point defects in solids. *Rev. Mod. Phys.* **2014**, *86* (1), 253–305. (b) Lee, C.; Scarpulla, M. A.; Ertekin, E. Investigation of Ga interstitial and vacancy diffusion in  $\beta$ -Ga<sub>2</sub>O<sub>3</sub> via split defects: a direct approach via master diffusion equations. *Phys. Rev. Mater.* **2024**, *8*, No. 054603.
- (34) Lany, S.; Zunger, A. Accurate prediction of defect properties in density functional supercell calculations. *Modell. Simul. Mater. Sci. Eng.* **2009**, *17* (8), No. 084002.
- (35) Chase, M. NIST-JANAF Thermochemical Tables, 4th ed.; American Institute of Physics, -1: 1998.
- (36) Waser, R.; Bieger, T.; Maier, J. Determination of acceptor concentrations and energy levels in oxides using an optoelectrochemical technique. *Solid State Commun.* **1990**, *76* (8), 1077–1081.
- (37) Rothschild, A.; Menesklou, W.; Tuller, H. L.; Ivers-Tiffée, E. Electronic Structure, Defect Chemistry, and Transport Properties of SrTi1-xFexO3-y Solid Solutions. *Chem. Mater.* **2006**, *18* (16), 3651–3659.
- (38) Ichihara, F.; Sieland, F.; Pang, H.; Philo, D.; Duong, A.-T.; Chang, K.; Kako, T.; Bahnemann, D. W.; Ye, J. Photogenerated Charge Carriers Dynamics on La- and/or Cr-Doped SrTiO3 Nanoparticles Studied by Transient Absorption Spectroscopy. *J. Phys. Chem. C* 2020, 124 (2), 1292–1302.
- (39) Claus, J.; Leonhardt, M.; Maier, J. Tracer diffusion and chemical diffusion of oxygen in acceptor doped SrTiO3. *J. Phys. Chem. Solids* **2000**, *61* (8), 1199–1207.
- (40) Alberi, K.; Scarpulla, M. A. Photoassisted physical vapor epitaxial growth of semiconductors: a review of light-induced modifications to growth processes. *J. Phys. D: Appl. Phys.* **2018**, *51* (2), No. 023001.
- (41) Wu, Y.; Bowes, P. C.; Baker, J. N.; Irving, D. L. Photochromism of UV-annealed Fe-doped SrTiO3. *Appl. Phys. Lett.* **2021**, *119* (26), No. 262901.

- (42) Kim, N.; Blankenau, B. J.; Su, T.; Perry, N. H.; Ertekin, E. Multisublattice cluster expansion study of short-range ordering in iron-substituted strontium titanate. *Comput. Mater. Sci.* **2022**, 202, No. 110969.
- (43) (a) Baker, J. N.; Bowes, P. C.; Long, D. M.; Moballegh, A.; Harris, J. S.; Dickey, E. C.; Irving, D. L. Defect mechanisms of coloration in Fe-doped SrTiO3 from first principles. *Appl. Phys. Lett.* **2017**, *110*, No. 122903. (b) Bowes, P. C.; Baker, J. N.; Irving, D. L. Survey of acceptor dopants in SrTiO3: Factors limiting room temperature hole concentration. *J. Am. Ceram. Soc.* **2020**, *103* (2), 1156–1173.
- (44) Alberi, K.; Scarpulla, M. A. Suppression of compensating native defect formation during semiconductor processing via excess carriers. *Sci. Rep.* **2016**, *6* (1), 27954.